

High-Power and High-Capacity Mobile Optical SWIPT

Mingliang Xiong, Qingwen Liu, *Senior Member, IEEE*, Shengli Zhou, *Fellow, IEEE*, Shun Han, Mingqing Liu, and Shengjie Zhao, *Senior Member, IEEE*

Abstract—The increasing demands of power supply and data rate for mobile devices promote the research of simultaneous information and power transfer (SWIPT). Optical SWIPT, as known as simultaneous light information and power transfer (SLIPT), can provide high-capacity communication and high-power charging. However, light emitting diodes (LEDs)-based SLIPT technologies have low efficiency due to energy dissipation over the air. Laser-based SLIPT technologies face the challenge in mobility, as it needs accurate positioning, fast beam steering, and real-time tracking. In this paper, we propose a mobile SLIPT scheme based on spatially separated laser resonator (SSLR) and intra-cavity second harmonic generation (SHG). The power and data are transferred via separated frequencies, while they share the same self-aligned resonant beam path, without the needs of receiver positioning and beam steering. We establish the analysis model of the resonant beam power and its second harmonic power. We also evaluate the system performance on deliverable power and channel capacity. Numerical results show that the proposed system can achieve watt-level battery charging power and above 20-bit/s/Hz communication capacity over 8-m distance, which satisfies the requirements of most indoor mobile devices.

Index Terms—SLIPT, resonant beam, laser communications, wireless power transfer, 6G mobile network.

I. INTRODUCTION

THE increasing demands of virtual reality (VR), augmented reality (AR), and other bandwidth-consuming services bring many challenges to conventional mobile networks, including radio frequency spectrum crisis and fast battery depletion. Simultaneous wireless information and power transfer (SWIPT) technology is an attractive way to cope with these challenges, as it can provide sustainable power supply through the communication link [1]. In the sixth-generation (6G) mobile network, SWIPT service is highly expected [2]. The final form of mobile network can be completely different from what we are experiencing today [3].

SWIPT using radio-frequency (RF) carrier has been widely studied. RF wave can provide a large coverage area and non-line-of-sight (NLoS) transmission; hence, it has many application scenarios. However, the shortage of RF spectrum resources has limited the development of RF-based SWIPT. To acquire high communication bandwidth, SWIPT based on light wave has arisen much attention [4]. Visible light

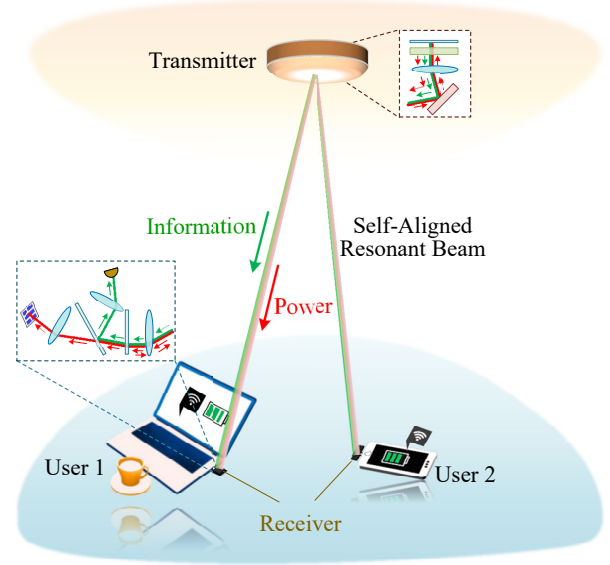


Fig. 1. Scenario of mobile optical SWIPT based on resonant beam

communication (VLC) technology has the potential to support over 1 Tbit/s data rate, which points out the promising prospect of optical SWIPT [5]. However, transmitters with isotropic antennas or light emitting diodes (LEDs) exhibit very low transmission efficiency due to the path loss over the large divergence angle. For example, an isotropic antenna operating at 900 MHz and supplied with 4-W source can only transfer $5.5 \mu\text{W}$ to the receiver at 15-m distance [6]. From LED radiation within 120° coverage angle, the receiver can only obtain 1.4-mW electric power at 1.5-m distance [7]. Therefore, for power-hungry devices, narrow-beam carrier is preferred. For instance, Iyer *et al.* demonstrated a laser power transfer system which can safely deliver over 2 W power at a range of 4.3 m [8]. Rizzo *et al.* employed 10-W 976-nm laser as the transmitter, achieving 2.37-W electricity output at the receiver [9]. Besides, hybrid optical wireless power and data transmission system is also introduced in [10].

Nevertheless, these laser-based optical SWIPT technologies face challenges in mobility, as they have to obtain the position of the receiver and then direct the laser beam to the receiver. Although beam steering can be realized by many non-mechanical devices, such as two-dimensional (2D) fiber arrays [11], in-fiber diffraction gratings [12], optical phased arrays (OPAs) [13], crossed gratings [14], and spatial light modulators (SLMs) [15], the positioning accuracy and scanning resolution may limit their performance in receiver tracking, especially for long-range transmission.

Resonant beam generated by spatially separated laser

M. Xiong and Q. Liu, S. Han, and M. Liu are with the College of Electronics and Information Engineering, Tongji University, Shanghai 201804, China (e-mail: xiongml@tongji.edu.cn; qliu@tongji.edu.cn; nuisthanshun@outlook.com; clare@tongji.edu.cn).

S. Zhou is with Department of Electrical and Computer Engineering, University of Connecticut, Storrs, CT 06250, USA (e-mail: shengli.zhou@uconn.edu).

S. Zhao is with the School of Software Engineering, Tongji University, China, and also with the Key Laboratory of Embedded System and Service Computing, Ministry of Education, Tongji University, Shanghai, 201804, China (email: shengjiezhao@tongji.edu.cn).

resonator (SSLR) can be used for mobile optical SWIPT without the requirements of positioning and beam steering, as shown in Fig. 1. Recently, high-power wireless charging using resonant beam was proposed in [16], which is known as resonant beam charging (RBC) or distributed laser charging (DLC). Experiment for DLC is demonstrated in [17]. Resonant beam communication (RBCom) system with high-capacity channel was illustrated in [18]. The primary structure of SSLR originates from Lindford's very long laser cavity which has two oppositely-placed corner cube retroreflectors [19]. The safety and mobility of the SSLR were verified in [20] and [21], respectively. The SSLR also has limitations with respect to communications, as the signal inside the cavity bounces back and forth, leading to echo interference. To address the echo interference issue, second harmonic generation (SHG) can be adopted to separate the communication carrier from the resonant beam; and for this concept, SSLR structures with external-cavity SHG and intra-cavity SHG are proposed in [22] and [23], respectively. Based on the aforementioned features of the RBC and RBCom system, SSLR-enabled SWIPT can provide both high-power mobile charging and high-capacity mobile communication.

Generally, receivers of optical SWIPT systems may use photon diodes (PDs) and/or photovoltaic panels (PVs) to convert light into current, and then use power splitting or time switching method to split the information stream and the power stream [3]. However, PDs which are widely used for information detection (ID) may not be suitable for energy harvesting (EH), while PVs are only suitable for EH due to its narrow bandwidth [24].

In this paper, we propose a resonant beam SWIPT (RB-SWIPT) system based on SSLR and intra-cavity SHG. In addition to the aforementioned advantages of the RBC and RBCom system in power, mobility, and capacity, the RB-SWIPT system separates the communication beam from the power transfer beam (i.e., the resonant beam) at the transmitter and converts them into current signal and electricity at the receiver independently using PDs and PVs.

The contributions of our work are as follows.

- 1) We propose the SHG-based RB-SWIPT system to provide a high-power and high-capacity mobile transmission channel, and design an optical frequency-splitting transmitting/independent conversion structure.
- 2) We establish the coupling model of the resonant beam power and its second harmonic power and analyze the performance of the RB-SWIPT system on the received charging power and channel capacity.

The remainder of this paper is organized as follows. Section II presents the system design of the RB-SWIPT system. Section III illustrates the system analysis model. Section IV demonstrates the results of performance evaluation. At last, we conclude in Section V.

II. THE PROPOSED SYSTEM

The SWIPT system is based on the SSLR and SHG scheme presented in [23]. As demonstrated in Fig. 2, power is transferred via 1064-nm resonant beam, while information is transferred via 531-nm frequency-doubled beam. The

frequency-doubled beam is generated from the resonant beam by an SHG crystal and modulated by an electro-optic modulator (EOM). At the receiver, part of the resonant beam is allowed to pass through mirror M2, and then is focused on the PV by lens L3. At last, the extracted resonant beam is converted to current by the PV to charge the battery. The frequency-doubled beam passes through M2, and then is separated from the resonant beam by a dichroic mirror M5; and finally, it is focused on the PD by lens L4 and converted to current by the PD.

The resonant beam is generated inside the SSLR cavity. The SSLR consists of two telecentric cat's eye retroreflectors (TCR) RR1 and RR2 which are placed at the transmitter and the receiver, respectively. Retroreflectors are devices to reflect the incident beam back to its incoming direction. Therefore, photons inside the SSLR cavity can oscillate between RR1 and RR2 regardless of the retroreflectors' location. Generally, a TCR consists of a lens and a rear mirror which are formed coaxially and separated with a space. The ray-transfer matrix of the telecentric cat's eye retroreflector is expressed as [23]

$$\begin{aligned} \mathbf{M}_{RR} &= \begin{bmatrix} 1 & f \\ 0 & 1 \end{bmatrix} \begin{bmatrix} 1 & 0 \\ -1/f & 1 \end{bmatrix} \begin{bmatrix} 1 & l \\ 0 & 1 \end{bmatrix} \begin{bmatrix} 1 & 0 \\ 0 & 1 \end{bmatrix} \begin{bmatrix} 1 & l \\ 0 & 1 \end{bmatrix} \\ &= \begin{bmatrix} 1 & 0 \\ -1/f & 1 \end{bmatrix} \begin{bmatrix} 1 & f \\ 0 & 1 \end{bmatrix} \\ &= \begin{bmatrix} 1 & 0 \\ -1/f_{RR} & 1 \end{bmatrix} \begin{bmatrix} -1 & 0 \\ 0 & -1 \end{bmatrix}, \end{aligned} \quad (1)$$

and

$$f_{RR} = \frac{f^2}{2(l-f)}, \quad (2)$$

where f is the focal length of the lens, and l is the interval between the lens and the mirror. If $l = f$, \mathbf{M}_{RR} represents an ideal TCR. The ray-transfer matrix of an optical system is used to calculate the position and the transfer direction of the output ray from parameters of the input ray. Given the vector of the input ray $[r_i, \alpha_i]^T$, we can obtain the vector of the output ray from an ideal TCR; that is

$$\begin{bmatrix} r_o \\ \alpha_o \end{bmatrix} = \mathbf{M}_{RR} \Big|_{l=f} \begin{bmatrix} r_i \\ \alpha_i \end{bmatrix} = \begin{bmatrix} -r_i \\ -\alpha_i \end{bmatrix}, \quad (3)$$

where r_i (r_o) and α_i (α_o) are the transverse displacement and the angle of the input (output) ray, respectively, with respect to the optical axis. From (3), we can see that the output ray is parallel to the input ray, as shown in Fig. 3. Nevertheless, in SSLR, l should be a little greater than f to ensure a stable resonator, which is illustrated in the following section. TCR has a pupil located at the focal point of the lens. Only the beams that pass through the pupil of the TCR can be retro-reflected. Therefore, the intra-cavity resonant beam always passes through the pupils of RR1 and RR2. We place the gain medium at the pupil of RR1, so that the resonant beam can pass through the gain medium regardless of the location of the receiver. Similarly, the EOM is placed behind the gain medium, so that the frequency-doubled beam can always pass through the EOM.

In this paper, we employ a neodymium-doped yttrium orthovanadate (Nd:YVO₄) crystal as the gain medium. This

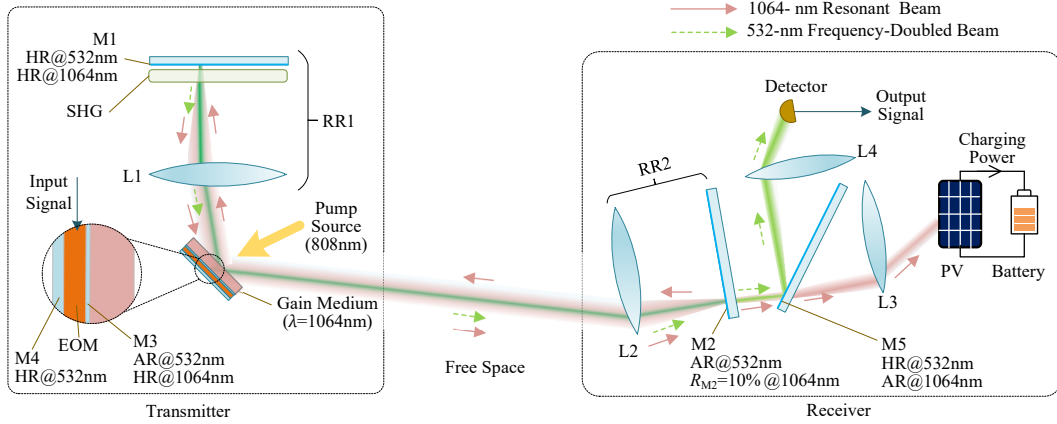


Fig. 2. Diagram of system structure (M1 and M2: mirrors; M3 and M4: coatings; M5: dichroic mirror; L1 to L4: lenses; RR1: the retroreflector at the transmitter, consisting of M1 and L1; RR2: the retroreflector at the receiver, consisting of M2 and L2; SHG: second harmonic generator; EOM: electro-optical modulator; PV: photovoltaic panel; AR: anti-reflective coating, i.e., transmittance $\approx 100\%$; HR: high-reflective coating, i.e., reflectivity $\approx 100\%$; M2 is partially reflective at 1064 nm with reflectivity of R_{M2})

material can amplify 1064-nm light wave under the irradiation of 808-nm pump source light. So, the intra-cavity resonant beam oscillating between RR1 and RR2 is amplified by the gain medium. Since the loss of the resonant beam is compensated by the gain, the resonance in the cavity can be maintained. SHG crystals are devices to generate frequency-doubled beam from a fundamental beam. In this system, the fundamental beam for SHG is the resonant beam. We place the SHG crystal inside RR1 and make it parallel to the rear mirror. Because beams that enter through the pupil of the TCR are perpendicular to the rear mirror, they have the same incident angle to the SHG crystal. This feature meets the phase-matching requirement of the SHG crystal.

Various anti-reflective (AR), high-reflective (HR), and partial-reflective coatings at different wavelengths are employed. M1 is coated with HR coating at 1064 nm. M2 is coated with partial-reflective coating at 1064 nm. Hence, M1 and M2 capture most of the resonant beam power. Only a small part of the resonant beam power is released by M2 for battery charging. The back side of the gain medium is coated with HR coating at 1064 nm to prevent the resonant beam passing through and being changed by the SHG crystal; and it is also coated with AR coating at 532 nm to allow the frequency-doubled beam going into the EOM. M1 and the back side of the EOM are coated with HR coatings at 532 nm to reflect the frequency-doubled beam. M2 is coated with AR coating at 532 nm to allow the frequency-doubled beam going out of the cavity, preventing any possible intra-cavity oscillation at 532 nm. The front side of M5 is coated with HR coating at 532 nm and AR coating at 1064 nm, so that M5 can separate the two wavelengths. Besides, the two sides of each lens and the SHG crystal, the input plane of the detector and the PV, and the back side of M5 are coated with AR coatings at both 1064 nm and 532 nm to prevent unnecessary reflection.

III. SYSTEM ANALYSIS

The proposed SWIPT system has two branches, i.e., the power transfer branch and the information transfer branch. In

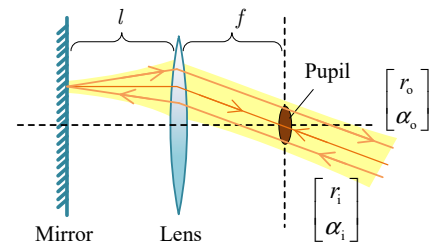


Fig. 3. Telecentric cat's eye retroreflector

this section, we at first introduce the mechanism of resonant beam generation, and present the necessary condition for a stable SSLR. Then, the process of generating the communication carrier is illustrated. At last, the photoelectric conversion and battery charging as well as the reception and detection of the information signal are described, respectively.

A. Resonant Beam Generation

In our system, the power is transferred via the resonant beam whose frequency is ν . As shown in Fig. 4(a), the resonant beam is generated between M1 and M2. In this work, we only consider that RR1 and RR2 have exactly the same parameters, including the same focal length f and the same space interval l . The beam radius $w(z)$ varies along the z -axis. The SSLR can be expressed with a single-pass ray-transfer matrix, which is also called the ABCD matrix; that is [22]

$$\begin{aligned} \begin{bmatrix} A & B \\ C & D \end{bmatrix} &= \begin{bmatrix} 1 & 0 \\ 0 & 1 \end{bmatrix} \begin{bmatrix} 1 & l \\ 0 & 1 \end{bmatrix} \begin{bmatrix} 1 & 0 \\ -1/f & 1 \end{bmatrix} \begin{bmatrix} 1 & 2f+d \\ 0 & 1 \end{bmatrix} \\ &= \begin{bmatrix} 1 & 0 \\ -1/f & 1 \end{bmatrix} \begin{bmatrix} 1 & l \\ 0 & 1 \end{bmatrix} \begin{bmatrix} 1 & 0 \\ 0 & 1 \end{bmatrix} \\ &= \begin{bmatrix} -1 - \frac{d}{f} + \frac{dl}{f^2} & 2f - 2l + d - \frac{2dl}{f} + \frac{dl^2}{f^2} \\ \frac{d}{f^2} & -1 - \frac{d}{f} + \frac{dl}{f^2} \end{bmatrix}, \end{aligned} \quad (4)$$

where d is the transmission distance that is defined as the space interval between the pupils of RR1 and RR2. The elements of ABCD matrix can be used to analyze the stability of resonators [25, 26]. Let $g_1^* = A$ and $g_2^* = D$, we can use the condition $0 < g_1^* g_2^* < 1$ to judge the stability of the SSLR. Using f_{RR} expressed in (2), we can know that the stable-cavity condition is $0 \leq d \leq 4f_{RR}$.

The components of the ABCD matrix can also be used to estimate the beam radius at arbitrary location along the optical axis. We should at first obtain the q -parameter and then use this q -parameter to calculate the beam radius. There are multiple transverse modes included in the resonant beam; and their superposition determines the radius of the resonant beam. The modes that can be included in a resonant beam are determined by the apertures of the optical devices in the cavity. Among these modes, the fundamental mode TEM_{00} exhibits the smallest radius. We can obtain the radius of the fundamental mode at location z by [27]

$$w_{00}(z) = \sqrt{-\frac{\lambda}{\pi \Im[1/q(z)]}}, \quad (5)$$

where $\Im[\cdot]$ takes the imaginary part of a complex number, and λ is the wavelength of the resonant beam. The $q(z)$ parameter is computed by [22]

$$q(z) = \begin{cases} jL^* \sqrt{\frac{g_2^*}{g_1^*(1-g_1^*g_2^*)}} + z, & z \in [0, z_{L1}] \\ \frac{q(z_{L1})}{-q(z_{L1})/f + 1} + (z - z_{L1}), & z \in (z_{L1}, z_{L2}] \\ \frac{q(z_{L2})}{-q(z_{L2})/f + 1} + (z - z_{L2}), & z \in (z_{L2}, z_{M2}] \end{cases} \quad (6)$$

where $L^* = B$, $z_{L1} = f$, $z_{L2} = l + 2f + d$, and $z_{M2} = 2l + 2f + d$ are the locations of L1, L2, and M2, respectively. From (6), we can observe that $q(z)$ is divided into three parts along z -axis. All the q -parameters are derived from $q(0)$. In fact, the q -parameters at one side of an optical element is derived from the q -parameters at the other side using ray-transfer matrices.

The ratio of the beam radius to the TEM_{00} radius is a constant along the z -axis. This ratio is called the beam propagation factor. To compute the beam radius $w(z)$ at arbitrary location z , we can firstly obtain the resonant beam radius $w(l+f)$ and the TEM_{00} mode radius $w_{00}(l+f)$ at the gain medium and then calculate the beam propagation factor. Since the aperture of the gain medium has the smallest aperture among the devices inside the cavity, we can consider that high-order modes whose radius is greater than the gain medium aperture are blocked, while only those with small radius remain in the cavity. Therefore, we can make a good approximation that $w(l+f) \approx a_g$, where a_g is the radius of the gain medium aperture [27]. Then the beam radius at location z can be computed by

$$w(z) = \frac{a_g}{w_{00}(l+f)} \sqrt{-\frac{\lambda}{\pi \Im[1/q(z)]}}. \quad (7)$$

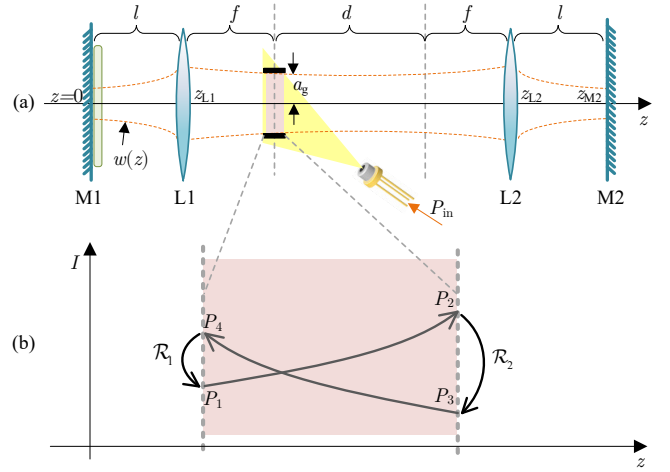


Fig. 4. System model for (a) intra-cavity beam radius and (b) intra-cavity circulating power

Next, we calculate the power of the resonant beam. The light wave bounces in the SSLR circularly, where the resonant beam power varies during transferring inside the SSLR. According to the Rigrod analysis, we can calculate the power at each stage, as depicted in Fig 4(b). Here, we create an equivalent resonator for this calculation, and assume that the beam radius in the gain medium is a fixed value. The equivalent resonator only contains two equivalent mirrors and a gain medium, as shown in Fig. 4(b). The reflectivity of the equivalent mirrors are \mathcal{R}_1 and \mathcal{R}_2 . Then, the power of the incident beam at the left-side equivalent mirror is obtained by [28]

$$P_4 = \frac{\pi a_g^2 I_s}{(1+r_1/r_2)(1-r_2 r_1)} \left[\frac{l_g \eta_c P_{in}}{I_s V} - \ln \frac{1}{r_2 r_1} \right], \quad (8)$$

where $r_1 \equiv \sqrt{\mathcal{R}_1}$ and $r_2 \equiv \sqrt{\mathcal{R}_2}$ are the voltage reflection coefficients of the equivalent mirrors, I_s is the saturation intensity, l_g is the gain medium thickness, η_c is the combined pumping efficiency, V is the gain medium volume, and P_{in} is the electric power for driving the pump source. \mathcal{R}_1 combines the power attenuation induced by the SHG and RR1. \mathcal{R}_2 combines the power attenuation induced by the gain medium, the air, and RR1. They are expressed as

$$\begin{cases} \mathcal{R}_1 = (1 - \eta_{SHG})^2 \Gamma_{SHG}^2 \Gamma_{RR1}, \\ \mathcal{R}_2 = \Gamma_g^2 \Gamma_{air}^2 \Gamma_{RR2} \Gamma_{diff}, \end{cases} \quad (9)$$

where η_{SHG} is the SHG efficiency which represents the consumption of the resonant beam power in the SHG process; Γ_{SHG} is the transmittance of the SHG crystal without considering the loss induced by the SHG process; Γ_{RR1} and Γ_{RR2} are the loss factors of RR1 and RR2, respectively; Γ_g is the transmittance of the gain medium; $\Gamma_{air} = \exp(-\alpha_{air} d)$ is the transmittance of the air, where $\alpha_{air} = 0.0001 \text{ m}^{-1}$ for clear air; Γ_{diff} is the diffraction loss factor which can be approximated by a closed-form formula presented in [22]. Γ_{RR1} is induced by the losses of passing through lens L1 and mirror M1. These losses mainly include the reflection of the surfaces of the lenses/crystals and the transmission of the

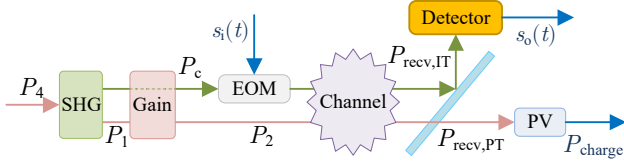


Fig. 5. Diagram of power and signal flows

mirrors, which are inevitable. Let Γ_{L1} denote the transmittance of L1, and R_{M1} denote the reflectivity of mirror M1, the loss factor of RR1 is expressed as

$$\Gamma_{RR1} = \Gamma_{L1}^2 R_{M1}. \quad (10)$$

Similarly, the loss factor of RR2 is expressed as

$$\Gamma_{RR2} = \Gamma_{L2}^2 R_{M2}, \quad (11)$$

where Γ_{L2} is the transmittance of lens L2, and R_{M2} is the reflectivity of mirror M2.

Now we have the expression of the resonant beam power at the left-side surface of the gain medium. Since the SHG efficiency η_{SHG} is a function of P_4 , we should solve the following equations to obtain the actual value of P_4 :

$$\begin{cases} P_4 = \frac{\pi a_g^2 I_s}{(1+r_1/r_2)(1-r_2r_1)} \left[\frac{l_g \eta_c P_{in}}{I_s V} - \ln \frac{1}{r_2 r_1} \right], \\ r_1 = (1 - \eta_{SHG}) \Gamma_{SHG} \sqrt{\Gamma_{RR1}}, \\ r_2 = \Gamma_g \Gamma_{air} \sqrt{\Gamma_{RR2} \Gamma_{diff}}, \\ \eta_{SHG} = \frac{8\pi^2 d_{eff}^2 l_s^2}{\varepsilon_0 c \lambda^2 n_0^3} \cdot \frac{2P_4}{\pi w^2(0)}, \end{cases} \quad (12)$$

where ε_0 is the vacuum permeability; c is the speed of light; d_{eff} , l_s , and n_0 are the SHG crystal's efficient nonlinear coefficient, thickness, and refractive index, respectively [29, 30]. Here, we assume the input of the SHG crystal is a plane wave. This is valid when l_s is smaller than the Rayleigh length $z_R = \pi w_0^2(0)/\lambda$, where $\lambda = c/\nu$ is the wavelength. Under this assumption, the beam radius is constant along the axis in the SHG crystal. $2P_4/[\pi w^2(0)]$ represents the resonant beam intensity that contains the leftward- and rightward-traveling wave at the SHG crystal. We also assume η_{SHG} is small, where the intensities of leftward- and the rightward-traveling waves at the SHG crystal are the same. This condition can be satisfied because the communication demand for the carrier beam power is very small. There is no analytic solution for (12). Hence, we obtain the numerical solution using MATLAB.

B. Communication Carrier Generation

The information carrier is the frequency-doubled (2ν) beam generated from the resonant beam by the SHG crystal. With the aforementioned low-SHG-efficiency assumption, the carrier beam power is approximated as

$$P_c = 2\eta_{SHG} P_4. \quad (13)$$

The carrier is the superposition of the frequency-doubled beams that generated from the leftward- and rightward-traveling components of the resonant beam. Generally, the SHG process is based on the nonlinear phenomenon of birefringent crystals, in which two fundamental photons interact with the crystal and then generate a frequency-doubled photon. Many materials, such as lithium niobate (LiNbO3), potassium titanyl phosphate (KTP), and potassium dihydrogen phosphate (KDP), can be employed for this purpose. Different materials exhibit different nonlinear coefficients and different phase matching angles. The incident angle of the input beam at the SHG crystal should be coincident with the phase matching angle to reach the maximum conversion efficiency. Since the beams between M1 and L1 are always perpendicular to these devices, a fixed beam incident angle at the SHG crystal can be satisfied. Hence, the crystal can be cut with proper orientation to ensure that the beam incident angle equals the phase matching angle.

C. Communication Channel and Capacity

As depicted in Fig. 2 and Fig. 5, the carrier is modulated by the EOM, transmitted through the channel, extracted by the dichroic mirror M5, and finally received by the detector. Along the transmission path, the signal is attenuated by the lenses, the mirrors, the gain medium, the EOM, and the air. These loss factors are caused by non-ideal reflection, non-ideal transmission, or absorption of impurity. Hence, the received optical power for information transfer is expressed as

$$P_{recv,IT} = \Gamma_{det} \Gamma_{L4} R_{M5}^{(2\nu)} \Gamma_{M2}^{(2\nu)} \Gamma_{L2} \Gamma_{air} \Gamma_{g,EOM} \Gamma_{L1} P_c, \quad (14)$$

where Γ_{M2} , Γ_{L2} , $\Gamma_{g,EOM}$, Γ_{air} , Γ_{L1} are the transmittances of M2, L2, the combined body of the gain medium and the EOM, the air, and L1, respectively; R_{M5} is the reflectivity of M5; the superscript (2ν) represents the acting frequency; Γ_{det} represents the actual percentage of the received power, not including the part that is reflected off the receiving plane.

From the received optical power to electric current, the conversion ratio is denoted by γ , which is usually called the PD's responsivity. Here we only consider the dominant noises, namely, the shot noise and the thermal noise. They are additive white Gaussian noise (AWGN). Hence, according to classical literature, the capacity of the communication channel is computed as [31, 32]

$$\tilde{C} = \log_2 \left\{ 1 + \frac{(\gamma P_{recv,IT})^2}{2e(\gamma P_{recv,IT} + I_{bk})B + \frac{4kTB}{R_{IL}}} \right\}, \quad (15)$$

where e is the electron charge, k is Boltzmann constant, $I_{bk} = 5100 \mu A$ is the photon current induced by background radiation [33], B is the bandwidth, T is the temperature in Kelvin, and R_{IL} is the load resistance.

D. Charging Power at Receiver

At the power transfer branch, the power P_2 of the traveling wave (at frequency ν) outputting off the right-side surface of the gain medium (see Fig. 4) is transferred through the channel and received by the PV panel. Similar to the

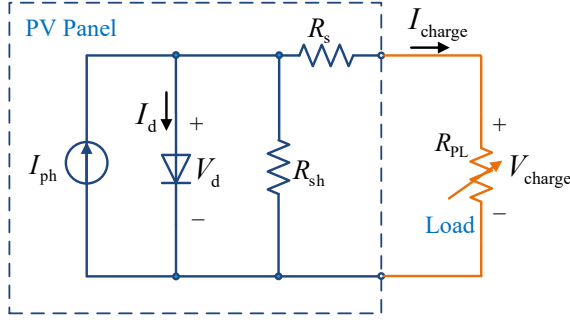


Fig. 6. Equivalent circuit model for PV panel

information transfer branch, the beam power experiences a series of attenuation induced by the air, L2, M2, M5, L3, and PV. Therefore, the received optical power for wireless charging is expressed as

$$P_{\text{recv,PT}} = \Gamma_{\text{PV}} \Gamma_{\text{L3}} \Gamma_{\text{M5}}^{(\nu)} \Gamma_{\text{M2}}^{(\nu)} \Gamma_{\text{L2}} \Gamma_{\text{air}} P_2, \quad (16)$$

where $P_2 = \pi a_g^2 I_2$; Γ_{L2} , Γ_{M2} , Γ_{M5} , and Γ_{L3} are the transmittance of L2, M2, M5, L3, respectively; and Γ_{PV} is the actual percentage of the received optical power by the PV from the total incident power, not including the part that is reflected off the PV's receiving plane. As shown in Fig. 4(b), the power P_2 and P_4 come from the amplification of P_1 and P_3 by the gain medium, respectively; and the power P_1 and P_3 come from the attenuation of P_4 and P_2 by the equivalent mirrors, respectively. Thus, the following relationships can be obtained:

$$\begin{cases} P_1 = \mathcal{R}_1 P_4, \\ P_3 = \mathcal{R}_2 P_2. \end{cases} \quad (17)$$

We also know that the production of the leftward- and rightward-traveling wave at arbitrary location in the z -axis is a constant, namely [28]

$$P_1 P_4 = P_2 P_3. \quad (18)$$

By combining these relationships expressed in (17) and (18), we can obtain

$$P_2 = \frac{r_1}{r_2} P_4. \quad (19)$$

Consequently, the received optical power at the power transfer branch can also be expressed as

$$P_{\text{recv,PT}} = \Gamma_{\text{PV}} \Gamma_{\text{L3}} \Gamma_{\text{M5}}^{(\nu)} \Gamma_{\text{M2}}^{(\nu)} \Gamma_{\text{L2}} \Gamma_{\text{air}} \left(\frac{r_1}{r_2} P_4 \right). \quad (20)$$

The received optical power at the PV panel is converted to electricity for battery charging. As demonstrated in Fig. 6, the PV panel can be equivalent to a current source in parallel with a diode. The current generated by the source is called the photo-current I_{ph} , which is related to the received optical power. The relation between the received optical power and the photo-current is expressed as

$$I_{\text{ph}} = \rho P_{\text{recv,PT}}, \quad (21)$$

where ρ is the optical-to-electrical conversion responsivity. However, for real devices, there are a shunt resistance R_{sh}

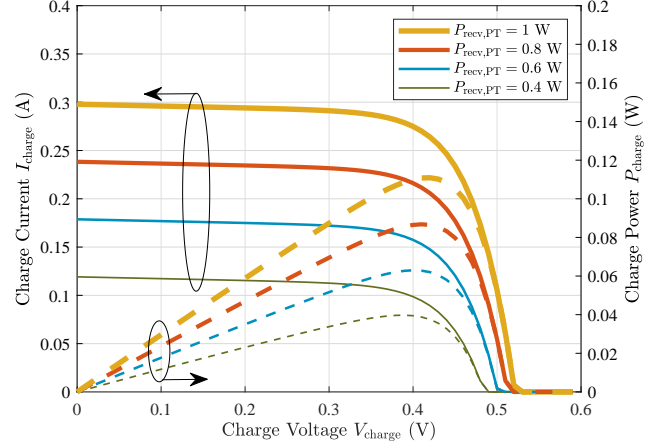


Fig. 7. Current-voltage and power-voltage characteristic curves of PV panel

TABLE I
PARAMETERS OF LASER RESONATOR [29, 34]

Parameter	Symbol	Value
Focal length of the lens	f	3 cm
Interval between the lens and mirror	l	3.015 cm
Saturation intensity of the gain medium	I_s	1.1976×10^7 W/m ²
Resonant beam wavelength	λ	1064 nm
Radius of gain medium aperture	a_g	2 mm
Gain medium thickness	l_g	1 mm
Combined pumping efficiency	η_c	43.9%
Efficient nonlinear coefficient	d_{eff}	4.7 pm/V
Refractive index of SHG crystal	n_0	2.23
SHG crystal thickness	l_s	0.2 mm
PV's responsivity	ρ	0.2981 A/W
Reverse saturation current	I_0	0.32 μ A
Shunt resistance	R_{sh}	53.82 Ω
Series resistance	R_s	37 m Ω
Diode ideality factor	n	1.48
Number of cells in PV panel	n_s	1
Temperature	T	298 K
PD's responsivity	γ	0.6 A/W
Load resistor	R_{TL}	10 k Ω

and a series resistance R_s component inside the PV model. According to Kirchhoff's law, we can write down the following equations for this circuit model; that is

$$\begin{cases} I_{\text{charge}} = I_{\text{ph}} - I_d - \frac{V_d}{R_{\text{sh}}}, \\ I_d = I_0 \left[\exp\left(\frac{V_d}{n_s n V_T}\right) - 1 \right], \\ V_d = I_{\text{charge}} (R_{\text{PL}} + R_s), \\ V_T = \frac{kT}{e}, \end{cases} \quad (22)$$

where I_d is the current passing through the diode; V_d is the voltage on the diode; I_0 is the reverse saturation current; k is Boltzmann's constant; n is the diode ideality factor; and n_s is the number of cells connected in series in the PV panel. In this paper, we only consider single-cell PV panel, i. e., we set

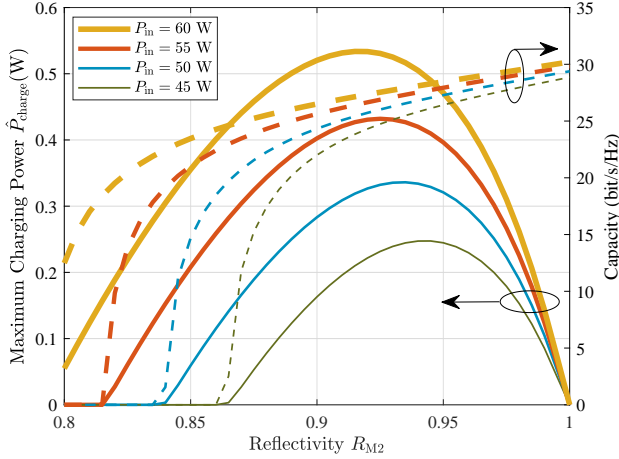


Fig. 8. Maximum charging power and channel capacity vs. reflectivity of mirror M2 (solid lines: maximum charging power; dashed lines: capacity; P_{in} : source power; distance $d = 6$ m; SHG crystal thickness $l_s = 0.2$ mm)

$n_s = 1$. We also obtain the numeric solution of (22), as it has no analytic solution.

Fig. 7 depicts the current-voltage (I-V) and power-voltage (P-V) characteristic curves of the PV panel. We can observe that for a certain $P_{recv,PT}$ the PV panel performs like a constant-current source until the output voltage V_{charge} reaches about 0.4 V. As V_{charge} continues to grow, the output current I_{charge} drops to zero quickly. Therefore, the PV can achieve a maximum power point (MPP) if we chose a proper charging voltage. Generally, this work is implemented by a maximum power point tracking (MPPT) device connected to the battery. To obtain the maximum charge power \hat{P}_{charge} , we solve the following problem

$$(P1): \hat{P}_{charge} = \max_{\{V_{charge}\}} I_{charge} V_{charge}, \quad (23)$$

$$\text{s.t.} \begin{cases} R_{PL} = \frac{V_{charge}}{I_{charge}}, \\ 0 \leq V_{charge} \leq V_{oc}, \end{cases} \quad (24)$$

In (24), R_{PL} is the equivalent load resistance of the circuit connected to the PV panel. It is the MPPT device that adjusts the load resistance automatically to find the MPP. V_{oc} is called the open-circuit voltage, which is the output voltage of the PV panel when no load circuit is connected.

IV. NUMERICAL RESULTS

A. Parameters Setting

In this paper, Nd:YVO₄ crystal is used as the gain medium. Hence, the wavelength of the resonant beam $\lambda = 1064$ nm, and the information carrier is the 532-nm frequency-doubled beam. Nd:YVO₄ is an efficient crystal for diode-pump solid-state lasers. It has large stimulated emission cross-section at lasing wavelength and high absorption coefficient at pumping wavelength. Thus, the crystal can be cut into a thin disk to satisfy the requirement of our system. The parameters of our system are listed in Table I. For devices through which the beams pass, including the lenses, the SHG crystal, and

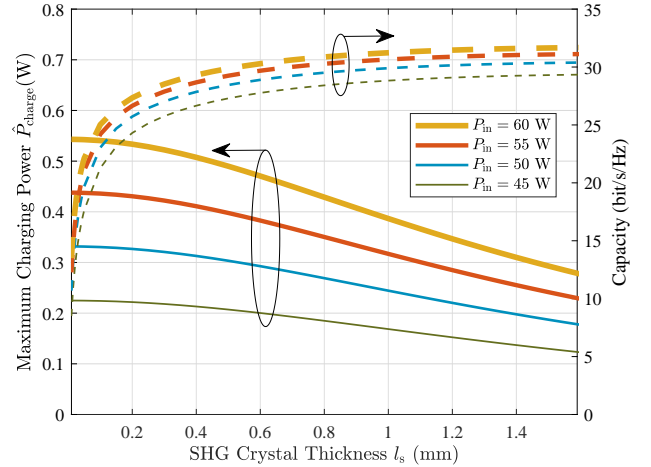


Fig. 9. Maximum charging power and channel capacity vs. SHG crystal thickness (solid lines: maximum charging power; dashed lines: capacity; P_{in} : source power; distance $d = 6$ m; M2's reflectivity $R_{M2} = 92\%$)

the dichroic mirror, unwanted reflection at their input and output surfaces exists even if these devices are with the best production. We assume the reflectivity at each AR surface is 0.5% which is an available value in the market. Therefore, we set $\{\Gamma_{L1}, \Gamma_{L2}, \Gamma_{L3}, \Gamma_{L4}, \Gamma_{SHG}, \Gamma_{M2}^{(2\nu)}, \Gamma_{M5}^{(\nu)}\} = 99\%$. Also the receiving surfaces of PD and PV have reflectivity of 0.5%; hence, we set $\{\Gamma_{det}, \Gamma_{PV}\} = 99.5\%$. HR mirrors/coatings also have inevitable transmittance; hence, we set their real reflectivity $\{R_{M1}, R_{M5}^{(2\nu)}\} = 99.5\%$. As the resonant beam passes the gain medium, it meets the front AR surface twice and the back HR surface once. Therefore, we set $\Gamma_g = 98.51\%$. The frequency-doubled beam meets interfaces five times as it passes the combined body of the gain medium and the EOM. Hence, we set $\Gamma_{g,EOM} = 97.52\%$. Besides, we set the bandwidth $B = 800$ MHz which is a feasible value of electro-absorption modulators [35]. The PV's parameters are obtained from [34].

B. Performance Evaluation

Fig. 8 demonstrates the maximum charging power \hat{P}_{charge} achieved by the MPPT device as a function of the reflectivity R_{M2} of the mirror M2, for different source power P_{in} . As R_{M2} increases, \hat{P}_{charge} gradually increases to a maximum point and then decreases to 0. The maximum value of \hat{P}_{charge} can be obtained with a specific R_{M2} . For instance, when $P_{in} = 60$ W, the maximum charging power can be obtained when R_{M2} is close to 92%. Moreover, as P_{in} grows, the optimal value of R_{M2} appears slightly decreasing. We also evaluate the communication capacity. As depicted in Fig. 8, with the increase of R_{M2} , the communication capacity increases rapidly at first; and when R_{M2} reaches a large value, the change gradually slows down. When $P_{in} = 60$ W and $R_{M2} = 92\%$, the maximum charging power \hat{P}_{charge} is 0.53 W and the channel capacity is over 27 bit/s/Hz.

Fig. 9 depicts the maximum charging power \hat{P}_{charge} and communication capacity as a function of the SHG crystal thickness l_s , for different source power P_{in} . According to (12),

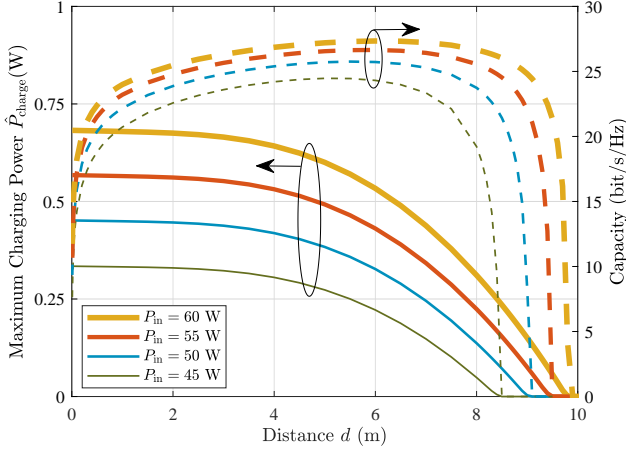


Fig. 10. Maximum charging power and channel capacity vs. distance (solid lines: maximum charging power; dashed lines: capacity; P_{in} : source power; M2's reflectivity $R_{M2} = 92\%$; SHG crystal thickness $l_s = 0.2$ mm)

the thickness of the SHG crystal l_s affects the SHG efficiency. As shown in Fig. 9, as l_s increases, the capacity increases rapidly at first and then gradually reaches the highest point. This is because the SHG efficiency increases with l_s , and therefore more frequency-doubled photons are generated. Conversely, the intra-cavity resonant beam power decreases gradually with the increase of the SHG efficiency, leading to the decrease of the maximum charging power.

In addition, we analyze the changes of the maximum charging power \hat{P}_{charge} and the communication capacity with the distance d , as shown in Fig. 10. With the increase of d , the maximum charging power decrease gradually. However, the capacity grows smoothly over most of the transmission range. This phenomenon can be explained by the reduction of the beam radius at the SHG crystal with the growth of d , which results in the increasing resonant beam intensity and SHG efficiency. When $P_{in} = 60$ W and the distance is less than 6 m, the maximum charging power keeps above 0.5 W, which is suitable for most indoor charging scenarios. For example, a typical mobile phone which is charged with 5 V 1 A (i.e., the charge power is 5 W) can be fully charged from 0% to 100% for 1 hour. When we use the RB-SWIPT system, the phone can be fully charged within 10 hours. Although the charging time is extended, the phone can be charged in use or in idle time, without the disturbing of cables. Similarly, the capacity keeps above 20 bits/s/Hz under most indoor circumstances. Only when d is less than 0.2 m or greater than 8 m does the capacity decrease rapidly.

From Fig. 11, the maximum charging power \hat{P}_{charge} and the communication capacity also depend on the source power P_{in} . There is a threshold of P_{in} for each case. If P_{in} is below the threshold, the resonance will not be established; and thus the charge power and the capacity are zeros. After P_{in} exceeds the threshold, \hat{P}_{charge} and the capacity start to increase. The capacity grows rapidly as P_{in} exceeds the threshold, and quickly reaches a slow growth rate. For a large range of P_{in} , the capacity can achieve over 20 bit/s/Hz. As P_{in} continues to increase, the growth rate of \hat{P}_{charge}

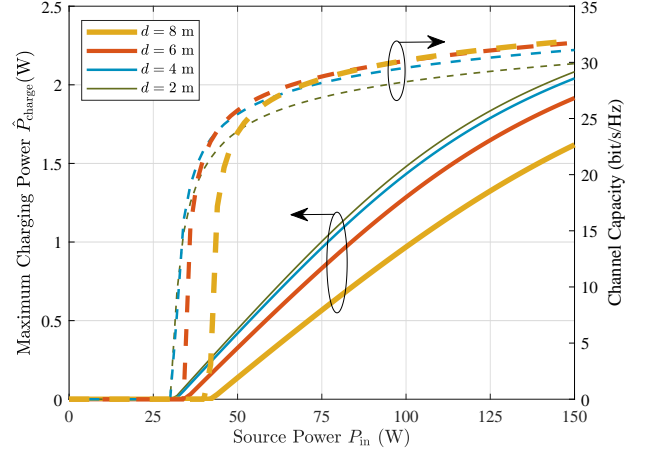


Fig. 11. Maximum charging power and channel capacity vs. source power (solid lines: maximum charging power; dashed lines: capacity; d : distance; M2's reflectivity $R_{M2} = 92\%$; SHG crystal thickness $l_s = 0.2$ mm)

reduces gradually. This phenomenon can be explained by the increasing SHG efficiency. Namely, with the increase of P_{in} , the resonant beam intensity at the SHG crystal keeps growing. Referring to (12), the SHG efficiency is positively related to the resonant beam intensity at the SHG crystal. Hence, more power of the resonant beam is converted to its second harmonic, resulting in the reduction of \hat{P}_{charge} . From Fig. 11, we can also observe that, by choosing an appropriate source power, the RB-SWIPT system can achieve watt-level power transfer over 8-m distance. The above performance can support most indoor mobile devices with permanent battery life and high-quality multimedia stream transmission.

V. CONCLUSIONS

In this paper, we proposed a resonant-beam-based simultaneous information and power transfer (RB-SWIPT) system which uses spatially separated laser resonator (SSLR) and second harmonic generation (SHG) to provide a high-power and high-capacity mobile transmission channel. We designed an optical frequency-splitting receiver structure, in which the power and information are transferred independently via the resonant beam and its frequency-doubled beam while sharing the same optical transmission path that is self-aligned without positioning and beam steering. We established the intra-cavity power coupling model of the resonant beam and the frequency doubled beam as well as the power receiving model to estimate the received battery charging power and the channel capacity. Numerical results show that the RB-SWIPT system can achieve watt-level battery charging and over 20-bit/s/Hz communication capacity for 8-m distance, which can enable permanent battery life and high-quality multimedia stream transmission of mobile devices in indoor scenarios.

REFERENCES

- [1] L. R. Varshney, "Transporting information and energy simultaneously," in *IEEE International Symposium on Information Theory*, Toronto, ON, Canada, July 2008, pp. 1612–1616.

- [2] K. David and H. Berndt, "6G vision and requirements: Is there any need for beyond 5G?" *IEEE Veh. Technol. Mag.*, vol. 13, no. 3, pp. 72–80, July 2018.
- [3] T. D. Ponnimbaduge Perera, D. N. K. Jayakody, S. K. Sharma, S. Chatzinotas, and J. Li, "Simultaneous wireless information and power transfer (SWIPT): Recent advances and future challenges," *IEEE Commun. Surveys Tuts.*, vol. 20, no. 1, pp. 264–302, Dec. 2018.
- [4] S. Ma, F. Zhang, H. Li, F. Zhou, Y. Wang, and S. Li, "Simultaneous lightwave information and power transfer in visible light communication systems," *IEEE Trans. on Wireless Communi.*, vol. 18, no. 12, pp. 5818–5830, Dec. 2019.
- [5] E. Ciaramella, Y. Arimoto, G. Contestabile, M. Presi, A. D'Errico, V. Guarino, and M. Matsumoto, "1.28-Tb/s (32×40 Gb/s) free-space optical WDM transmission system," *IEEE Photon. Technol. Lett.*, vol. 21, no. 16, pp. 1121–1123, Aug. 2009.
- [6] T. Le, K. Mayaram, and T. Fiez, "Efficient far-field radio frequency energy harvesting for passively powered sensor networks," *IEEE J. Solid-State Circuits*, vol. 43, no. 5, pp. 1287–1302, May 2008.
- [7] P. D. Diamantoulakis and G. K. Karagiannidis, "Simultaneous lightwave information and power transfer (SLIPT) for indoor IoT applications," in *IEEE Global Communications Conference*, Singapore, Dec. 2017, pp. 1–6.
- [8] V. Iyer, E. Bayati, R. Nandakumar, A. Majumdar, and S. Gollakota, "Charging a smartphone across a room using lasers," *Proc. ACM Interact. Mob. Wearable Ubiquitous Technol.*, vol. 1, no. 4, pp. 1–21, Jan. 2017.
- [9] L. Rizzo, K. J. Duncan, J. L. Zunino, and J. F. Federici, "Validation of laser power beaming applications with enlarged laser beam diameters minimizing hazardous operation," in *SoutheastCon*, Huntsville, AL, USA, Apr. 2019, pp. 1–5.
- [10] A. W. S. Putra, H. Kato, and T. Maruyama, "Hybrid optical wireless power and data transmission system," in *IEEE PELS Workshop on Emerging Technologies: Wireless Power Transfer (WoW)*, Seoul, Korea (South), Nov. 2020, pp. 374–376.
- [11] T. Koonen, A. Khalid, J. Oh, F. Gomez-Agis, and E. Tangdionga, "High-capacity optical wireless communication using 2-dimensional IR beam steering," in *Opto-Electronics and Communications Conference (OECC) and Photonics Global Conference (PGC)*, Singapore, Nov. 2017, pp. 1–4.
- [12] G. Wang, U. Habib, Z. Yan, N. J. Gomes, Q. Sui, J.-B. Wang, L. Zhang, and C. Wang, "Highly efficient optical beam steering using an in-fiber diffraction grating for full duplex indoor optical wireless communication," *J. Lightw. Technol.*, vol. 36, no. 19, pp. 4618–4625, Oct. 2018.
- [13] H. Rhee, J. You, H. Yoon, K. Han, M. Kim, B. G. Lee, S. Kim, and H. Park, "32 Gbps data transmission with 2D beam-steering using a silicon optical phased array," *IEEE Photon. Technol. Lett.*, vol. 32, no. 13, pp. 803–806, May 2020.
- [14] T. Koonen, J. Oh, K. Mekonnen, and E. Tangdionga, "Ultra-high capacity indoor optical wireless communication using steered pencil beams," in *Proc. International Topical Meeting on Microwave Photonics*, Paphos, Cyprus, Oct. 2015, pp. 4802–4809.
- [15] Z. Zhang, J. Dang, L. Wu, H. Wang, J. Xia, W. Lei, J. Wang, and X. You, "Optical mobile communications: Principles, implementation, and performance analysis," *IEEE Trans. Vehi. Technol.*, vol. 68, no. 1, pp. 471–482, Nov. 2019.
- [16] Q. Liu, J. Wu, P. Xia, S. Zhao, W. Chen, Y. Yang, and L. Hanzo, "Charging unplugged: Will distributed laser charging for mobile wireless power transfer work?" *IEEE Veh. Technol. Mag.*, vol. 11, no. 4, pp. 36–45, Nov. 2016.
- [17] W. Wang, Q. Zhang, H. Lin, M. Liu, X. Liang, and Q. Liu, "Wireless energy transmission channel modeling in resonant beam charging for IoT devices," *IEEE Internet Things J.*, vol. 6, no. 2, pp. 3976–3986, Jan. 2019.
- [18] M. Xiong, Q. Liu, G. Wang, G. B. Giannakis, and C. Huang, "Resonant beam communications: Principles and designs," *IEEE Commun. Mag.*, vol. 57, no. 10, pp. 34–39, Oct. 2019.
- [19] G. J. Linford, E. R. Peressini, W. R. Sooy, and M. L. Spaeth, "Very long lasers," *Appl. Opt.*, vol. 13, no. 2, pp. 379–390, Feb. 1974.
- [20] W. Fang, H. Deng, Q. Liu, M. Liu, Q. Jiang, L. Yang, and G. B. Giannakis, "Safety analysis of long-range and high-power wireless power transfer using resonant beam," *IEEE Trans. Signal Process.*, vol. 69, pp. 2833–2843, May 2021.
- [21] M. Liu, M. Xiong, Q. Liu, S. Zhou, and H. Deng, "Mobility-enhanced simultaneous lightwave information and power transfer," *IEEE Trans. Wireless Commun.*, 2021, to appear, doi=10.1109/TWC.2021.3078808.
- [22] M. Xiong, M. Liu, Q. Jiang, J. Zhou, Q. Liu, and H. Deng, "Retro-reflective beam communications with spatially separated laser resonator," *IEEE Trans. Wireless Commun.*, 2021, to appear, doi=10.1109/TWC.2021.3062945.
- [23] M. Xiong, Q. Liu, X. Wang, S. Zhou, B. Zhou, and Z. Bu, "Mobile Optical Communications Using Second Harmonic of Intra-Cavity Laser," *arXiv e-prints*, pp. 1–22, June 2021. [Online]. Available: <https://arxiv.org/abs/2106.11116>
- [24] G. Pan, P. D. Diamantoulakis, Z. Ma, Z. Ding, and G. K. Karagiannidis, "Simultaneous lightwave information and power transfer: Policies, techniques, and future directions," *IEEE Access*, vol. 7, pp. 28 250–28 257, Feb. 2019.
- [25] H. Kogelnik, "Imaging of optical modes — resonators with internal lenses," *Bell Syst. Tech. J.*, vol. 44, no. 3, pp. 455–494, July 1969.
- [26] P. Baues, "Huygens' principle in inhomogeneous, isotropic media and a general integral equation applicable to optical resonators," *Opt. Quantum Electron.*, vol. 1, no. 1, pp. 37–44, Feb. 1969.
- [27] N. Hodgson and H. Weber, *Laser Resonators and Beam Propagation: Fundamentals, Advanced Concepts and Applications 2nd ed.* New York, NY, U.S.: Springer, 2005.
- [28] A. E. Siegman, *Lasers*. Mill Valley, CA: University Science Books, 1986.
- [29] W. Koechner, *Solid-State Laser Engineering, 6th ed.* New York, NY, USA: Springer, 2006.
- [30] U. Simon and F. K. Tittel, "Nonlinear optical frequency conversion techniques," *Experimental Methods in the Physical Sciences*, vol. 29, no. 08, pp. 231–278, Jan. 1997.
- [31] A. K. Majumdar, *Advanced Free Space Optics (FSO)*. New York, NY, USA: Springer, 2015.
- [32] F. Xu, M. A. Khalighi, and S. Bourennane, "Impact of different noise sources on the performance of PIN- and APD-based FSO receivers," in *Proceedings of the 11th International Conference on Telecommunications*, Graz, Austria, June 2012, pp. 211–218.
- [33] A. J. C. Moreira, T. V. Rui, and A. M. de Oliveira Duarte, "Optical interference produced by artificial light," *Wirel. Netw.*, vol. 3, no. 2, pp. 131–140, May 1997.
- [34] W. Long, T. Wu, J. Jiao, M. Tang, and M. Xu, "Refraction-learning-based whale optimization algorithm for high-dimensional problems and parameter estimation of PV model," *Eng. Appl. Artif. Intell.*, vol. 89, p. 103457, Mar. 2020.
- [35] C. Quintana, Q. Wang, D. Jakonis, X. Piao, G. Erry, D. Platt, Y. Thueux, A. Gomez, G. Faulkner, and H. Chun, "High speed electro-absorption modulator for long range retroreflective free space optics," *IEEE Photon. Technol. Lett.*, vol. 29, no. 9, pp. 707–710, May 2017.